Journal of Hydrology 402 (2011) 25–40

Contents lists available at ScienceDirect

Journal of Hydrology

journal homepage: www.elsevier.com/locate/jhydrol

Comparison of roughness models to simulate overland flow and tracer transport experiments under simulated rainfall at plot scale

C. Mügler [a,*], O. Planchon [b], J. Patin [a], S. Weill [a,1], N. Silvera [c], P. Richard [d], E. Mouche [a]

[a] Laboratoire des Sciences du Climat et de l'Environnement, UMR 8212 CEA-CNRS-UVSQ, Orme des Merisiers, 91191 Gif-sur-Yvette Cedex, France
[b] Institut de Recherche pour le Développement, UMR LISAH, 2 Place Viala, F-34060 Montpellier Cedex 1, France
[c] Institut de Recherche pour le Développement, UMR BIOEMCO, LDD Office of Science & Land Development 2003/61 Pahon Yothin Road, Chatuchak 10900 Bangkok, Thailand
[d] Institut National de la Recherche Agronomique, UMR BIOEMCO, Campus AgroParisTech, Batiment EGER, 78850 Thiverval-Grignon, France

ARTICLE INFO

Article history:
Received 26 October 2010
Received in revised form 11 February 2011
Accepted 26 February 2011
Available online 10 March 2011
This manuscript was handled by K.P. Georgakakos, Editor-in-Chief, with the assistance of Attilio Castellarin, Associate Editor

Keywords:
Rainfall-simulation
Tracer injection
Roughness model
Friction law

SUMMARY

The Saint-Venant equations have consistently proved capable of accurately simulating hydrographs at plot scale. However, recent works showed that even though the hydrograph is satisfyingly reproduced, the flow velocity field within the plot might be wrong, with the highest velocity largely underestimated. Moreover, the choice of roughness models to be used in the Saint-Venant equations is most often done in the purpose of increasing the hydrograph quality, while the actual travel time of water is ignored. This paper presents a tracer experiment made on a 10-m by 4-m rainfall simulation plot, where travel time and tracer mass recovery as well as local flow velocity have been measured. Four roughness models are tested: (i) Darcy-Weisbach's model, (ii) Lawrence's model, (iii) Manning's model with a constant roughness coefficient, and (iv) Manning's model with a variable roughness coefficient which decreases as a power law of the runoff water depth.

Models with a constant friction factor largely underestimate high velocities. Moreover, they are not able to simulate tracer travel-times. Lawrence's model correctly simulates low and high velocities as well as tracer breakthrough curves. However, a specific set of parameters are required for each breakthrough curve from the same experiment. The best results are obtained with the Manning's model with a water-depth dependent roughness coefficient: simulated velocities are consistent with measurements, and a single set of parameters captures the entire set of breakthrough curves, as well as tracer mass recovery.

The study reported here brings the following findings: (i) roughness coefficient is flow-dependent, (ii) faithful simulation of the velocity fields does not imply a good prediction of travel time and mass recovery, (iii) the best model is a Manning type model with a roughness coefficient which decreases as a power law of water depth.

The full dataset used in this work is available on request. It can be used as benchmark for overland flow and transport models.

1. Introduction

Overland flow and transport of sediments, dissolved nutrients or contaminants in runoff water depth are important processes involved in water erosion and pollution. Modelling transport of sediments and chemicals requires accurate calculation of flow velocity. In hydraulic models, the hydraulic resistance, characterized by a roughness parameter, is one of the key parameters which determine runoff water depth and overland flow distribution. Many equations relate velocity to friction slope (Kirby, 1978). A general formulation of the friction law expresses velocity as a function of flow depth and friction slope, as follows:

$$u_i = \alpha h^{\beta} \sqrt{S_{fi}}, \tag{1}$$

where u_i is the i-component of the local depth-averaged velocities ($i = x$ or y), h the local water depth and S_{fi} the friction slope in the i-direction. An appropriate choice of parameters α and β leads to the following familiar relationships:

- Chezy's relationship with $\beta = 1/2$ and α equal to the Chezy's resistance parameter;
- Darcy-Weisbach's relationship with $\beta = 1/2$ and $\alpha = (8g/f)^{1/2}$, where f is the Darcy-Weisbach's friction factor, proportional to the ratio of gravity to inertial forces;
- Manning-Strickler's friction law with $\beta = 2/3$ and $\alpha = 1/n$ where n is the Manning's roughness coefficient representing hydraulic resistance to flow.

* Corresponding author.
E-mail address: claude.mugler@cea.fr (C. Mügler).
[1] Present address: Laboratoire d'Hydrologie et de Géochimie de Strasbourg, UMR 7517 CNRS, Université de Strasbourg, 1 rue Blessig, 67084 Strasbourg Cedex, France.

0022-1694/$ - see front matter © 2011 Elsevier B.V. All rights reserved.
doi:10.1016/j.jhydrol.2011.02.032

Chezy and Manning equations were originally developed in the purpose of sizing canals in the XIXth century (Mouret, 1921). Darcy-Weisbach equation was initially developed for pipe flow. These equations assume numerous restrictive conditions: flow is uniform, parallel to the surface, flow width is constant, grain roughness is homogeneous over the wetted perimeter and can be considered as random. None of the former conditions are met in overland flow (Smith et al., 2007). Nevertheless, Chezy, Manning and Darcy-Weisbach equations are the most widely used for calculating flow velocity in runoff and erosion models.

In the case of one-dimensional flow through pipes, the Reynolds number, which measures the relative significance of inertia and viscosity ($Re = 4uh/v$ where v is the fluid kinematic viscosity), is an important dimensionless number to estimate the friction coefficient. Indeed, in laminar regime, the friction factor is inversely proportional to the Reynolds number, while in turbulent regime (i.e. at Reynolds numbers greater than 2000 in pipe flows) it is determined by the roughness ratio. According to Lawrence (1997), the Reynolds number at which the roughness ratio becomes dominant is much smaller for overland flow in presence of macroscale roughness than it is for classical pipe flow. Furthermore, previous experimental studies of resistance to overland flow on desert hillslopes (Abrahams et al., 1986) suggested that the conventional *f-Re* relationship for shallow flow over a plane bed whose shape is a function of the state of flow did not apply to desert hillslopes and should not be employed in mathematical models of overland flow on such hillslopes. As a consequence, Lawrence (1997) proposes to use the inundation ratio rather than the flow Reynolds number for modelling the hydraulics of overland flow on rough granular surfaces. The inundation ratio describes the average submergence of soil surface roughness. It is used to categorize flow regime into partially inundated, marginally inundated and well-inundated surfaces. Each category is characterized by a functional relationship which expresses the frictional resistance as a function of the inundation ratio. The author defines Λ, a dimensionless degree of inundation of a rough surface: $\Lambda = h/h_c$, where h is flow depth and h_c the characteristic roughness scale of the surface. In the literature, the surface roughness h_c is often equal to $d_{50}/2$ or $d_{90}/2$ where d_{50} and d_{90} are the median-weight diameter and 90%-weight diameter of the particle size distribution, respectively (Abrahams et al., 1986; Lawrence, 1997).

At partial inundation, when flow depth is less than the mean roughness height, flow resistance is associated with the drag force derived from individual roughness elements and increases with depth and percentage cover according to (Lawrence, 1997):

$$f = \frac{8PC_D}{\pi} min\left(\frac{\pi}{4}, \Lambda\right), \tag{2}$$

where C_D is the drag coefficient for roughness elements and $min[a, b]$ is used to refer for the minimum value of either expression a or b. In Eq. (2), P is the fractional cover or portion of the surface covered by the largest particles. In (Lawrence, 1997), C_D is assumed to be constant and equal to 1 although in (Lawrence, 2000), at partial inundation, C_D decreases with percentage cover.

At marginal inundation, when roughness elements are fully covered but their height has the same magnitude as flow depth, the ratio of the size of roughness elements to the depth of flow controls the degree of vertical mixing in the flow. Consequently, frictional resistance sharply decreases with increasing flow depth (Lawrence, 1997):

$$f = \frac{10}{\Lambda^2}. \tag{3}$$

Well-inundated flows, in which water depth is significantly greater than roughness height, are described by using rough turbulent flow hydraulics previously developed for open channel flows. These flows exhibit a much more gradual decrease in frictional resistance with increasing depth than during the marginal inundation regime (Lawrence, 1997):

$$f = \frac{1}{(1.64 + 0.803 \times ln\Lambda)^2}. \tag{4}$$

Despite the existence of more sophisticated models such as the heuristic physical Lawrence's model, Manning's roughness coefficient n (see Eq. (1) with $\beta = 2/3$ and $\alpha = 1/n$) is still often used for shallow water overland flow, where it is assumed constant in time and independent of flow depth. Manning's coefficient depends on soil type and vegetative cover (De Roo et al., 1989; Jain and Singh, 2005). Katul et al. (2002) showed that when the water depth is much larger than the characteristic soil roughness height, Manning's roughness coefficient n can be calculated from

$$n = 0.06(z_0)^{1/7}, \tag{5}$$

where z_0 is the momentum roughness height, defined as the bed-normal location of zero-velocity predicted by the "log-law" approximation of the velocity profile in the Prandtl-Karman mixing-length theory. This relationship between n and z_0 is used by Thompson et al. (2010), among others, to estimate Manning's friction factor of an idealized one-dimensional hillslope with uniform sinusoidal microtopography with fixed amplitude A. They assume that z_0 scales linearly with the fixed depression height $2A$. In the case of vegetative cover, several authors showed that the vegetative resistance varies with flow depth or the degree of submergence. For example, Wu et al. (1999) concluded from analysis of experimental data that the vegetative roughness coefficient of un-submerged vegetation reduces with increasing flow depth and is independent of bed slope. They also pointed out that the vegetative roughness coefficient of fully submerged vegetation tends to increase at low depths but then decrease to an asymptotic constant as the water level continues to rise. Tsihrintzis (2001) showed that most of these experimental data can be modelled with the Kadlec's power law for flow through vegetation (Kadlec, 1990). So, Jain et al. (2004) adopted such a simplified form of depth-dependent roughness formulation in a distributed rainfall–runoff model:

$$n = n_0\left(\frac{h}{h_0}\right)^{-\varepsilon} \quad \text{for } h < h_0 \text{ and } n = n_0 \quad \text{for } h \geqslant h_0, \tag{6}$$

where n is depth-dependent Manning's roughness coefficient, n_0 is the minimum land surface-dependent Manning's roughness corresponding to flow depth h_0 beyond which n is assumed constant. ε is an exponent related to vegetation drag. With this model, the authors obtained numerical results for both temporal variations of the spatial distribution of flow depth and runoff over a catchment in fairly good agreement with measurements. Rai et al. (2010) also used a power law for the depth-dependent overland flow resistance. They showed that variable roughness preserved the hydrograph shape better than constant one.

The objective of this study is to compare different roughness models:

- Darcy-Weisbach (DW)'s model;
- Lawrence's model;
- Manning's model with constant roughness coefficient;
- Manning's model with a water-depth dependent roughness coefficient.

In order to test these models, a rainfall simulation experiment was held in Thies, Senegal. It was done with an improved version of the large rainfall simulator (4-m by 10-m) described by Esteves et al. (2000a). The experiment aimed at measuring both local flow velocity within the plot and breakthrough curves of point-source

injection of tracer. Because the two measurements could not be done during the same rainfall (see materials and methods section for details), two rainfall simulations have been successively done. The first one was devoted to capture the tracer breakthrough curves and mass recovery of tracer injected in several points of the plot. This rainfall simulation will be called the transport experiment. The next rainfall was devoted to local flow velocity measurements. We will call it the surface runoff experiment. The later has already been published (Tatard et al., 2008). In the present paper, the entire dataset is used. A dedicated code was written in order to achieve the desired comparison. Comparison with Tatard's et al. (2008) preliminary results is made when appropriate.

It must be emphasized that this type of joint model calibration on a flow and a transport experiment is fairly common in hydrogeology (Bear et al., 1993). Among such studies, the single fracture system with matrix diffusion (Grisak and Pickens, 1981) is a typical example of such studies, as well as a good analogue of the plot problem targeted in the present study. The literature on fracture models shows that the joint calibration of flow and transport is generally difficult to achieve: a good calibration of the flow model, i.e. of the transmissivity field, linked to the roughness of the fracture plane, leads to a poor calibration of the breakthrough curve and vice versa (Andersson et al., 2004). More recently, joint calibrations of runoff hydrograph and tracer measurements has also been done in hillslope hydrology. For example, McGuire et al. (2007) used a spatially explicit model constrained by soil hydrologic properties, runoff and applied tracer data to identify the dominant processes necessary to explain both water and solute flux from a steep hillslope. To the best knowledge of the authors, no attempt has been done in surface hydrology to do a joint calibration of local flow velocities and tracer breakthrough curves at the plot scale. According to the above cited literature in hydrogeology, the exercise promised challenging, as well as possibly very selective with regard to the selected roughness models.

In this paper, the materials and methods section presents the experiments and the four models. The results section presents the calibration of the surface runoff experiment with the four models, followed by the corresponding operation for the transport experiment. Models are compared to each other. This comparison is followed by a general discussion of the relative performance of the tested models. Especially, we discuss why the power Manning model, which is in essence a phenomenological model[2] performed better than the Lawrence model, which is in essence a physically-based model.[3]

2. Materials and methods

2.1. Experiments

The rainfall simulation experiment was held in Thies, Senegal. The plot was 10 m long by 4 m wide, with a 1% slope, and sandy soil (1% clay, 7% silt, 43% fine sand, 49% coarse sand). The granulometry of the sandy soil is given in Table 1. The rainfall simulator was as described by Esteves et al. (2000a). It allowed for rainfall at a constant average intensity of 70 mm h^{-1}. In order to limit wind effects, which may cause noticeable variations of rainfall intensity, simulations were carried out at a maximum wind speed of 1 m s^{-1}. Six tipping-bucket rain gauges with electronic recording were placed along the plot borders for monitoring the actual rainfall intensity. The flow discharge was collected in a trough and alternately directed, via a 10-cm flexible hose, into two 150-l iron cylinders, one being filled while the other was drained. The volume in the filling cylinders was monitored by recording the rise of a float. The resolution of this apparatus was 2.5 l. The typical flow discharge at steady state was 0.5 l s^{-1}.

Table 1
Granulometry of the sandy soil.

Grain size (μm)	50	100	150	200	250	500	750
Portion (%)	4	13	15	14	13	32	5

Table 2
Chronology of plot preparation and experiments.

Day from start	Work done
0	Initial rainfall in order to moisten the soil
1	Plot preparation: removing 5 cm at the surface already polluted by previous experiments, plowing upside-down the next 50 cm, adding fresh surface soil to replace the removed layer Raking and forming the V shape
2	Two hours of rainfall in order to produce an already 'old' surface, which was supposed to evolve much slower than the raked one
3	Microtopography measurement
4	Transport experiment
5	Microtopography measurement
6	First (unsuccessful) attempt of surface runoff experiment
7	Microtopography measurement
8	Surface runoff experiment (Tatard et al., 2008)
9	Microtopography measurement + high resolution photography for further mosaicing

2.1.1. Plot preparation

Table 2 gives the chronology of plot preparation and experiments. On day 1 of the experiment, plot preparation consisted on manual plough of the plot to a depth of 50 cm. The surface was then raked in order to form a slight V shape, with 1% slope longitudinally and 1% slope towards the median axis of the plot. The purpose of the V shape was to avoid rill development at the edge of the plot. On day 2 of the experiment (see Table 2), a 2-hour long rainfall was applied at a constant intensity of 70 mm h^{-1}. Rainfall intensity of 70 mm h^{-1} is common in the region (return time in the order of a year). However, a duration of 2 hours at this intensity has no possible point of comparison with natural rainfall. The experiment was designed in order to maintain steady runoff and infiltration rate during enough time to perform the flow velocity measurements. In this purpose, several hours of rainfall had been applied on the plot prior to the experiment in order to form an already 'old' surface with a well organized flow pattern that would erode very slowly during the experiment itself. The longitudinal slope had evolved from straight to slightly concave with some sand deposits in the concave downstream. Fig. 1 gives a general view of the plot. Days 3 and 5 were devoted to soil microtopography measurements. They were done with an automated device described in Planchon et al. (2000). It consists of a vertical rod with a sensor at the end that detects the soil surface. Stepper motors allow the apparatus to move in small increments in all directions. The horizontal resolution is 2.5 cm transversally to the plot and 5 cm longitudinally. The vertical precision is 0.5 mm. With a maximum acquisition rate of 1.6 point s^{-1}, the 16,000 measured points of the entire Digital Elevation Model (DEM) required a full working day. The calculation of the Random Roughness with a formulation which simultaneously removes slope and tillage effects (Planchon

[2] We call a phenomenological model a model based on empirial laws inspired by field observations. These laws are derived after being introduced in the conservation laws of Physics (mass, momentum, and/or others).

[3] We call a physically-based model a model which describes as faithfully as possible the true physics of an idealized, simplified, and often uniformized vision of reality.

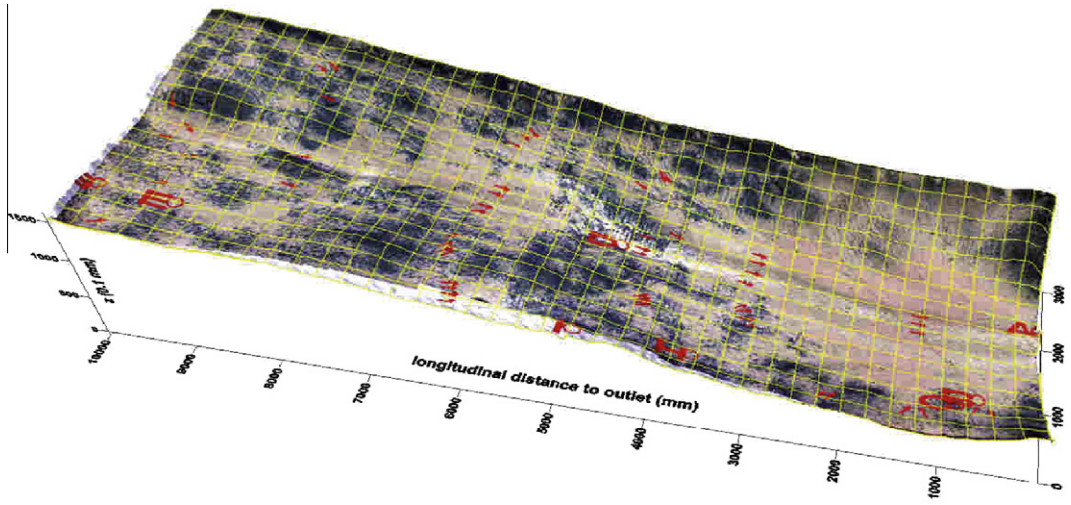

Fig. 1. General view of the plot. Horizontal coordinates are in mm. Vertical scale is magnified 10 times. Colour contrast and saturation are artificially enhanced in order to highlight the surface feature pattern which is tiny in reality, although important for understanding the plot behaviour and evolution. Arrows show flow velocity measured points during the surface runoff experiment. Letters show the injection points in the transport experiments. The grid space is 25 cm. Topography and overland image used in the figure were captured at the end of all experiments. The small, narrow, bright part at the middle of the right-hand side of the plot corresponds to missing data in the image mosaic (only elevation is known there).

et al., 2001) leads to a value lying between 0.5 mm and 2.5 mm depending on the considered zone in the plot.

2.1.2. Transport experiment

Although surface runoff experiments usually come first in numerical-versus-experimental works in hydrodynamics, we chose to perform the transport experiment first because the carbon chlorite used in the surface runoff experiment, even in the small quantities we needed (see Tatard et al., 2008), was prone to pollute the plot, which would jeopardize any further tracing experiment. Contrarily, even a significant pollution by tracers would not affect local velocity measurements. The tracer used was a mixture of $H_2{}^{18}O$ (5 g), ^2H_2O (5 g), $CaCl_2(6H_2O)$ (250 g) and KBr (15 g). A small and unknown quantity of water added to this composition because of $CaCl_2$ hygroscopicity. The bulk density of the final solution was 1437 kg m^{-3}. Each injection consisted in applying 1 g s^{-1} of tracer during 30 s at a predetermined point chosen from the DEM acquired the day before. Injection of tracer started after a time of 30 mn of rainfall, when the discharge had stabilized. Tracer was injected at eight locations in the plot, noted A to I in Fig. 1 (see also Fig. 6). The upper-stream locations (C, G) were chosen at source points of runoff (i.e. where no runoff could come from upstream). Locations D and E were in the main channel. Other injection points were on small, but clearly visible flow path. Location A, the most downstream point set at the outlet of the plot, was devoted to the characterization of the response of the experimental setup between the outlet of the plot and the sampling bottles. The experiment on day 4 (see Table 2) consisted of a 1h24'-long continuous rainfall at constant rainfall intensity (75 ± 5 mm h^{-1}). At the outlet of the plot, a peristaltic pump diverted a constant 20-ml s^{-1} flow, from the runoff water, into a silicon hose which served at collecting manually one sample at every second. Additionally, a conductivity sensor was plugged at the mouth of the hose, thus giving in real time the apparent conductivity of each one-second sample. The term apparent conductivity means that the sensor, which had to be handcraft in order to fit in the hose, was not calibrated. Further calibration of the conductivity measurement was done by comparison with ^{18}O analysis. The sensor was then proved linear and accurate. At the end of rainfall, all samples were hermetically sealed for further ^{18}O and ^2H isotopic analysis.

Uncertainties of tracer measurements can be estimated from the following considerations:

- Time synchronization between all operations was supervised by an operator with a whistle, which typically allowed a time uncertainty of ±1 s.
- The overall mass of tracer injected at every location was known with high precision by weighting the remaining tracer before and after every injection.
- The mass of tracer in each one-second sample was measured by real-time apparent conductivity measurement. After the experiment, ^{18}O has been measured in 131 samples, the exact mass of tracer has been deduced from these and compared to the corresponding apparent conductivity measurement. The comparison gave a linear relation between tracer mass and conductivity (r^2 = 0.985), which corresponds to an uncertainty of ±3% on the mass in each single one-second sample.

2.1.3. Surface runoff experiment

The surface runoff experiment was described by Tatard et al. (2008). In essence, it consists in a miniaturized version of the salt velocity gauge (SVG) presented in Planchon et al. (2005). Two conductivity probes of 1-cm wide each are posted at exactly 10 cm to each other in the exact flow direction. Salt brine is injected manually a few centimetres upstream to the upper probe. Electric conductivity is measured simultaneously at the two probes at 250 Hz during 2.5 s. Velocity is obtained by inverse modelling of the 1D transport model of the brine between the two probes. 72 points were measured with one to three replications. These points were selected with the following objectives: (i) to cover the largest range of flow velocity as allowed with the SVG technology (i.e. 0.005–1 m s^{-1}) and, (ii) to be scattered within the entire plot.

Field problems as well as failure or poor quality of the inversion model brought the need of filtering the data in order to be certain to reject erroneous measurements. This was done thanks to additional data recorded by the device, such as peak height, root mean square error (RMSE) of the inverse model. The accuracy of the SVG technology observed in ideal conditions is typically ±2.5% (Darboux, 2011). In our experimental conditions, uncertainties on

velocity measurement can be estimated from the replications of measurement at the same location. From these, it appears that the best measuring conditions (standard deviation of 0.8 cm s^{-1}) occurred when velocity was below 3 cm s^{-1} or above 15 cm s^{-1}. The worst measuring conditions appeared at 5 cm s^{-1}, with a standard deviation of 1.4 cm s^{-1}. At the end, 62 mean local velocity measurements at 62 individual points were selected for further use.

2.2. Models

2.2.1. General equations

Overland flow is usually described by the depth-averaged two-dimensional unsteady flow equations commonly referred to as the Saint-Venant equations (Zhang and Cundy, 1989; Esteves et al., 2000b). They consist of balance equations for the mass of water (Eq. (7)), and for the flow momentum, the later being written for each planar-coordinate directions x (Eq. (8)) and y (Eq. (9)). They can be written as:

$$\frac{\partial h}{\partial t}+\frac{\partial(u_x h)}{\partial x}+\frac{\partial(u_y h)}{\partial y}=R-I, \tag{7}$$

$$\frac{\partial u_x}{\partial t}+u_x\frac{\partial u_x}{\partial x}+u_y\frac{\partial u_x}{\partial y}+g\left(\frac{\partial h}{\partial x}+S_{fx}-S_{ox}\right)=0, \tag{8}$$

$$\frac{\partial u_y}{\partial t}+u_x\frac{\partial u_y}{\partial x}+u_y\frac{\partial u_y}{\partial y}+g\left(\frac{\partial h}{\partial y}+S_{fy}-S_{oy}\right)=0, \tag{9}$$

where h is the local water depth, u_x and u_y the x- and y-components of the local depth-averaged velocities, R the rainfall intensity, I the infiltration rate and g the gravitational constant. S_{0x} and S_{fx} (resp. S_{0y} and S_{fy}) are the ground slopes and the friction slopes in the x- and y-directions, respectively.

Tracer transport in the water depth is described by the following depth-averaged advective–dispersive equation (Weill et al., 2009):

$$\frac{\partial hc}{\partial t}+\vec{\nabla}.(h\vec{u}c-\overline{\overline{D}}\overrightarrow{\nabla c})=q_c, \tag{10}$$

where h is the local water depth, c the depth-averaged concentration, $\vec{u}$ the runoff velocity, $\overline{\overline{D}}$ the surface diffusion-dispersion tensor and q_c a source or sink of concentration. In the followings, q_c, equal to the product $-Ic$, represents the sink of concentration due to infiltration. The diffusion-dispersion tensor can be written as:

$$\overline{\overline{D}}=h\overline{\overline{d_1}}+h\overline{\overline{d_2}}|\vec{u}|, \tag{11}$$

where $\overline{\overline{d_1}}$ and $\overline{\overline{d_2}}$ are the diffusion tensor and the surface dispersivity tensor, respectively.

2.2.2. Diffusive-wave approximation

Processes of overland flow and channel flow are usually modelled using approximations of the Saint-Venant equations based on the diffusive and the kinematic wave models (Chow et al., 1988).

In the diffusive-wave approximation, inertia terms are neglected and the momentum balance equations (8) and (9) reduce to:

$$S_{fi}=S_{oi}-\frac{\partial h}{\partial x_i}, \tag{12}$$

where i stands for the x and y-horizontal directions. Following Wasantha Lal (1998) and according to Weill et al. (2009), this equation becomes:

$$S_{fi}=-\nabla_i(h+z_l), \tag{13}$$

where z_l is the land surface elevation, defined such that the soil topographic slope is equal to $-\nabla_i z_l$. Physical attenuation due to local and convective accelerations and due to lateral inflow perpendicular to flow direction is not accounted for in the diffusive wave approximation. However, there is still some physical dissipation due to the spatial change in flow depth.

In the kinematic-wave approximation, however, all terms in the momentum equations (8) and (9) which cause the wave energy to dissipate as it moves downstream are neglected and Eqs. (8) and (9) reduce to equate friction and bed slope:

$$S_{fi}=S_{oi}. \tag{14}$$

Woolhiser and Liggett (1967) introduced dimensionless forms of the Saint-Venant equations which involve only two dimensionless parameters: the Froude number F and the kinematic-wave number k, defined as:

$$F=\frac{u_0}{\sqrt{gh_0}}, \tag{15}$$

$$k=\frac{S_0 L_0}{h_0 F^2}, \tag{16}$$

where u_0 and h_0 are the depth-averaged velocity and the normal water depth at $y=L_0$, respectively. The kinematic-wave approximation is applicable to very steep slopes. Woolhiser and Liggett (1967) recommend this approximation whenever $k>20$. This criterion has later been modified by Morris and Woolhiser (1980) to $kF^2>5$ when $F<0.5$ and $k>20$ when $F>0.5$. Pearson (1989) suggests a new criterion for using the kinematic-wave approximation to the Saint-Venant equations for steady-state shallow water flow: $k>3+5/F^2$. Finally, the calculation of actual amounts of errors of kinematic-wave and diffusive-wave approximations for steady-state overland flows led to the conclusion that for small values of kF^2, the diffusive-wave approximation should be preferred over the kinematic-wave approximation (Singh and Aravamuthan, 1996; Moussa and Bocquillon, 1996, 2000).

In the experimental configuration studied in the present paper and already described in (Tatard et al., 2008), the maximum water depths h_0 measured on the plot ranged between 1 cm and 2 cm. Deepest water were located in the middle of the plot ($L_0=5$ m). The measured velocities were 0.25 and 0.15 m s^{-1}, respectively.

Table 3
Characteristics of the four different models.

Model	Friction factor $f(h)$	Parameters
Darcy-Weisbach (DW)	$f(h)=cste=f$	f
Lawrence	for $0<h<h_c/4$, $f(h)=(8P/h_c)\times h$ for $h_c/4<h<(5/P)^{1/2}h_c$, $f(h)=2P$ for $(5/P)^{1/2}h_c<h$, $f(h)=min(10\times h_c/h)^2,(1.64+0.803\times ln(h/h_c))^{-2})$	P and h_c
Manning with constant n	$f(h)=8gn^2/h^{1/3}$	n
Manning with variable $n(h)$	$f(h)=8g(n(h)^2)/h^{1/3}$ with $n(h)=n_0\times(h/h_0)^-$ with limit $n\geqslant n_0$	n_0, h_0, ε

The value of the Froude and kinematic-wave numbers were 0.8 (resp. 0.3) and 8 (resp. 22) for $h_0 = 1$ cm and 2 cm, respectively. The product $(k-3)F^2$ was consequently less than 5, which falls within the range of validity of the diffusive-wave approximation for modelling this data set.

As done in (Weill et al., 2009), assuming that the water depth gradient is much smaller than the surface elevation gradient, the friction law given by Eq. (1) may be written as a function of the mean local slope S as follows:

$$u_i = -\frac{\alpha h^{\beta}}{\sqrt{S}} \nabla_i (z_l + h). \tag{17}$$

Introducing this equation in Eq. (7) leads to the following diffusive-wave equation for overland flow:

$$\frac{\partial h}{\partial t} - \vec{\nabla} \cdot \left(\frac{\alpha h^{\beta+1}}{\sqrt{S}} \right) \vec{\nabla} (z_l + h) = R - I. \tag{18}$$

Numerical simulations presented in the following sections are for steady state flow only (see the end of the following paragraph for details). This allowed us to assume both rainfall intensity R and infiltration rate I constant in space and time. R and I were therefore not explicitly computed. Comparison (not reported here) between our results and a fully coupled model solving diffusive equation and Richards equation on the entire hydrograph (Weill, 2007) showed that these assumptions were justified.

Table 4
Calibrated parameter values and corresponding RMSE for each model.

Model	Calibrated parameter values	RMSE (m s^{-1})
Darcy-Weisbach (DW)	$f = 0.2$	3.2×10^{-2}
Lawrence	$P = 30\%$ and $h_c = 0.25$ mm	2.8×10^{-2}
Manning with constant n	$n = 0.02$	3.1×10^{-2}
Manning with variable $n(h)$	$n_0 = 0.013$, $h_0 = 3$ mm, $\varepsilon = 1/3$	2.6×10^{-2}
PSEM_2D with constant f	$f = 0.26$	3.1×10^{-2}
PSEM_2D with variable f	see Tatard et al. (2008)	3.1×10^{-2}

2.2.3. Friction factors

In this paper, we compare four models characterized by the same friction law Eq. (1) with $\beta = 1/2$ and $\alpha = (8g/f(h))^{1/2}$, but with the following expressions for the friction factors $f(h)$:

- $f(h) = cste$. This model is called Darcy-Weisbach (DW)'s model further on in the paper. It is characterized by the constant value of f.
- $f(h)$ given by Eqs. (2)–(4). This model is called Lawrence's model. It is characterized by the values of the characteristic roughness scale h_c and fractional cover P.
- $f(h) = 8gn^2/h^{1/3}$. This model is called Manning's model with a constant n. It is characterized by the value of Manning's coefficient n.
- $f(h) = 8g(n(h))^2/h^{1/3}$. This model is called Manning's model with a variable n. Even if we investigated a bare soil in the present paper, we have adopted the Manning's water-depth dependent coefficient $n(h)$ given by Eq. (6) and used by Jain et al. (2004) to model overland flow in a vegetated catchment. This model is characterized by the values of minimum Manning's roughness n_0, exponent ε and flow depth h_0 beyond which n is assumed constant.

Characteristics of each model are summarized in Table 3.

The models were solved with the numerical code (Cast3M) developed by the French Atomic Energy Commission (CEA) (see the website www-cast3m.cea.fr for more information). A Mixed-Hybrid Finite Element (MHFE) formulation was used to solve the overland flow Eq. (18) and transport Eq. (10) (Dabbene, 1998; Bernard-Michel et al., 2004). The time discretization was implicit. Calculations were performed in two steps: the steady state overland flow was solved first. The tracer experiment was computed by using the steady state formerly calculated. One can notice that

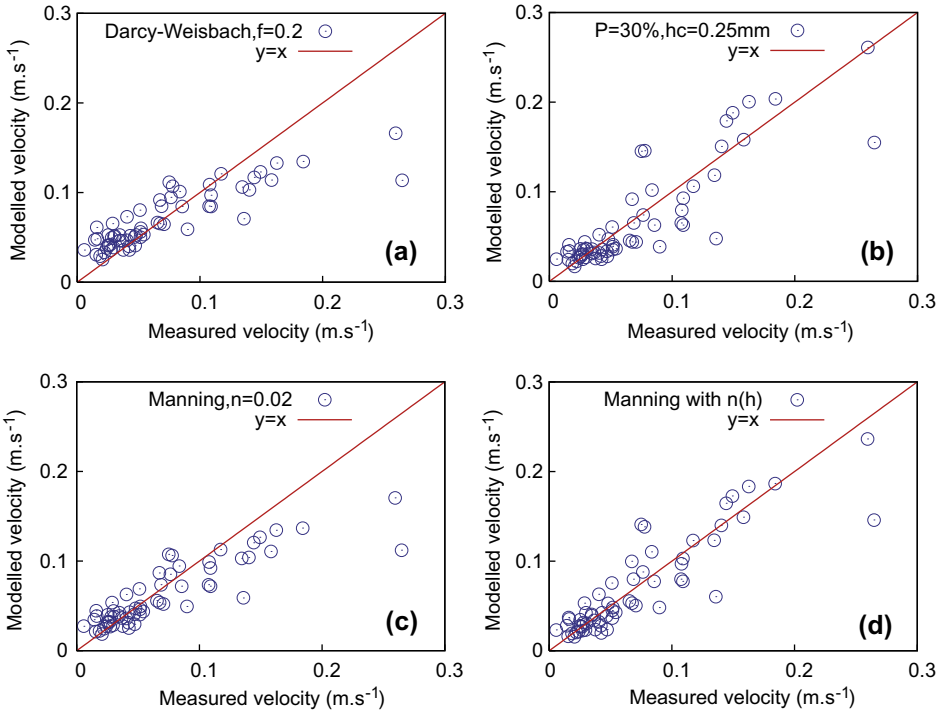

Fig. 2. Modelled versus measured velocities for four different friction laws: (a) Darcy-Weisbach's model with a constant friction factor f equal to 0.2; (b) Lawrence's model with $P = 30\%$ and $h_c = 0.25$ mm; (c) Manning's model with a constant n equal to 0.02; (d) Manning's model with $n(h)$ given by Eq. (6) where $n_0 = 0.013$, $h_0 = 3$ mm and $\varepsilon = 1/3$.

neither the rise nor the fall of the experimental hydrographs were used in the present work.

3. Results

3.1. Surface runoff experiment

To model the surface runoff experiment, we used the same DEM (made of $10 \times 10\,cm^2$ cells) as Tatard et al. (2008) used with the code PSEM_2D. The parameters involved in the expression of the friction factor (see Table 3) were calibrated from the minimisation of the root mean square error (RMSE) which quantifies the global agreement between the simulated and the measured velocities. The RMSE is defined as follows:

$$RMSE = \sqrt{\frac{1}{N}\sum_{i=1}^{N}(u_{obs,i} - u_{sim,i})^2}, \tag{19}$$

where $u_{obs,i}$ and $u_{sim,i}$ are the observed and simulated velocities at the location i. The total number of locations N was equal to 62. In

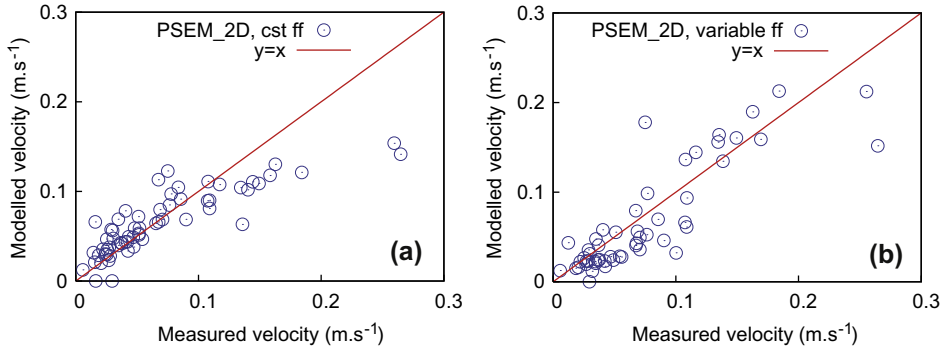

Fig. 3. Modelled versus measured velocities obtained from PSEM_2D with: (a) a constant friction factor f, (b) a varying friction factor f (see Figs. 4 and 5 in (Tatard et al., 2008)).

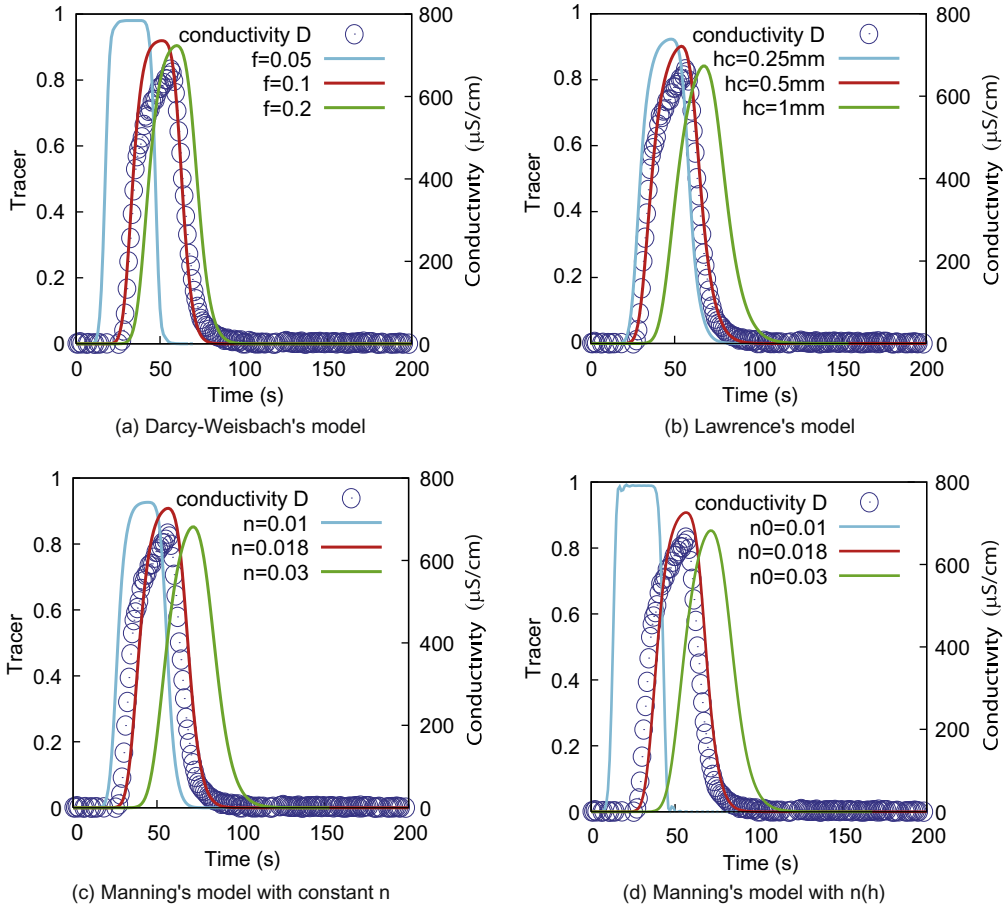

Fig. 4. Calibration of the four friction models from breakthrough curve of tracer injected in the main rill (point D). Best results are obtained with (a) $f = 0.1$ for Darcy-Weisbach's model; (b) $h_c = 0.5$ mm for Lawrence's model (no influence of parameter P); (c) $n = 0.018$ for Manning's model with constant n; (d) $n_0 = 0.018$ for Manning's model with variable $n(h)$.

Table 5
Parameter values used to simulate transport experiments for each model.

Model	Injection at D	Injection at E	Injection at G	Injection at I	Injection at H
Darcy-Weisbach	$f = 0.1$	$f = 0.2$	$f = 0.4$	$f = 0.4$	$f = 0.6$
Lawrence	$h_c = 0.5$ mm	$h_c = 0.5$ mm	$h_c = 0.5$ mm	$h_c = 0.5$ mm	$h_c = 0.5$ mm
	no influence of P	$P = 13\%$	$P = 30\%$	$P = 30\%$	$P = 100\%$
Manning with constant n	$n = 0.018$	$n = 0.018$	$n = 0.025$	$n = 0.025$	$n = 0.03$
Manning with variable $n(h)$	$n_0 = 0.018$	$n_0 = 0.018$	$n_0 = 0.018$	$n_0 = 0.018$	$n_0 = 0.018$
	$h_0 = 3$ mm	$h_0 = 3$ mm	$h_0 = 3$ mm	$h_0 = 3$ mm	$h_0 = 3$ mm
	$\varepsilon = 1/3$	$\varepsilon = 1/3$	$\varepsilon = 1/3$	$\varepsilon = 1/3$	$\varepsilon = 1/3$

calibration exercises, the calibrated parameter values are usually not unique and are slightly dependent on the type of objective criteria used. However, perhaps because of the large number of measurements, we did not have to face any problem of equifinality.

As presented in Table 4, calibration gave $f = 0.2$ for DW's model, $n = 0.02$ for Manning's model, $P = 30\%$ and $h_c = 0.25$ mm for Lawrence's model and $n_0 = 0.013$, $h_0 = 3$ mm and $\varepsilon = 1/3$ for Manning's model with $n(h)$. Parameters P and h_c involved in the expression of the friction factor for Lawrence's model could have been directly deduced from soil characteristics. The soil used in the Thies experiment was mainly made of fine and coarse sands which granulometry is given in Table 1. The percentage covered by large grains of 500-μm diameter was equal to 32% and only 5% of sand was made of larger grains of 750-μm diameter. The d_{90} value, equal to 0.5 mm, gives a theoretical characteristic roughness h_c equal to 0.25 mm. Finally, experimental values for Lawrence's model parameters should be: $P = 32\%$ and $h_c = 0.25$ mm, values which are very close to those obtained from calibration. Modelled velocities compared to observed ones are given in Fig. 2.

3.2. Transport experiment

3.2.1. Calibration

In this section and the followings, we call "breakthrough curve for injection point P" the experimental breakthrough curve of tracer injected at point P (P = A to I in Fig. 6) and measured at the plot outlet. Model calibration is performed from the tracer arrival time and tracer mass recovery.

High-resolution flow-velocity measurements presented and modelled in previous section were performed 4 days after the tracer measurements (see Table 2). During these 4 days, a 2-hour simulated rainfall slightly modified topography, and more consistently plot roughness. DEMs used to model surface runoff experiment and transport experiment were therefore slightly different. Furthermore, the modelling of the transport experiment was performed on the measured topographic data (5 cm longitudinally, i.e. along the plot slope, and 2.5 cm transversely). Additional simulations (not reported here) with a coarser grid (10×10 cm^2 cells) showed that, compared to fine grid simulations, smoothing artificially plot roughness increased flow velocity and, correlatively, made tracers to arrive earlier at the outlet. Furthermore, simulations performed with the microtopography measured 1 day after the experiment showed a strong modification of tracer arrival times when the tracer is injected near to the bottom of the plot (injection points B and C, Fig. 6). This can be due to a real modification of the microrelief: erosion smoothes the area where water flow is fast. It also may be related to the presence of the trough where flow is collected, and which disturbs the topography. Consequently, in the following, we will disregard breakthrough curves for injection points B and C. Breakthrough curve for injection point A was only useful to estimate the fluid travel time between the plot outlet and the sampling bottles. Finally, we present in this section the breakthrough curves for the five injection points D, E, G, H and I. As the topography changed, parameters involved in the expression of friction factors for the different models and calibrated from the surface runoff experiment are no more valid for the transport experiments and have to be calibrated again. As in previous sections, the four models used for the friction factor are DW's model, Lawrence's model and Manning's model both with a constant n or a variable $n(h)$ (see Table 3). The steady state of the hydraulic equation Eq. (18) was then solved for all models and model parameters were calibrated from the breakthrough curve of tracer injected in the main rill (point D). Indeed, when injected at point D, the tracer travels in zones where the velocity and the water depth are large and it allows us to calibrate flow parameters from high-velocity zones. The purpose of this paper is not to perform a precise calibration of all parameters but rather to compare their behaviour to each other. So, for the transport experiment, we performed a qualitative calibration from a finite number of high-resolution simulations.

Fig. 4 gives the evolution versus time of both the measured conductivity and the modelled tracer concentration at the plot outlet for injection point D and the four different models. Optimised parameter values are summarized in the first column of Table 5. The calibrated friction factor f for DW's model is equal to 0.1. As the tracer injected at D only travels in zones where water depth is large, the friction factor modelled with Lawrence's model is given by Eq. (3) and does not depend on the percentage cover P. In Fig. 4(b), the percentage cover is fixed to 30% and three various values of the characteristic roughness h_c are investigated. The best agreement with experimental measurements is obtained with $h_c = 0.5$ mm. This h_c value is two times larger than the value deduced from d_{90} and used in the previous section to model local velocities but is comparable with the calculated Random Roughness of the plot. Roughness is not only determined by the largest sand particles but also by the microtopography formed at the plot surface by previous rainfalls, such as very small furrows of millimetric mean depth.

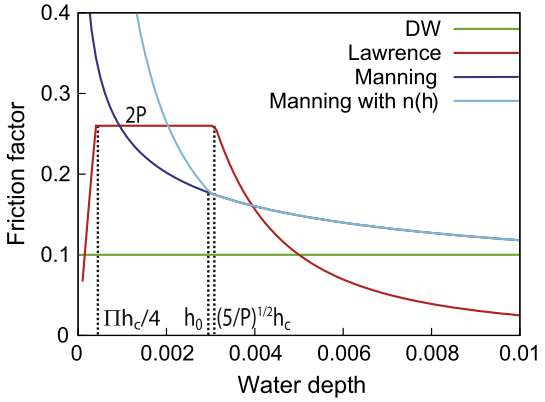

Fig. 5. Friction factor as a function of water depth according to Darcy-Weisbach's model with $f = 0.1$ (green curve), Lawrence's model with $P = 13\%$ and $h_c = 0.5$ mm (red curve), Manning's model with $n = 0.018$ (blue curve) and Manning's model with $n(h)$ given by Eq. (6) with $n_0 = 0.018$, $h_0 = 3$ mm and $\varepsilon = 1/3$.

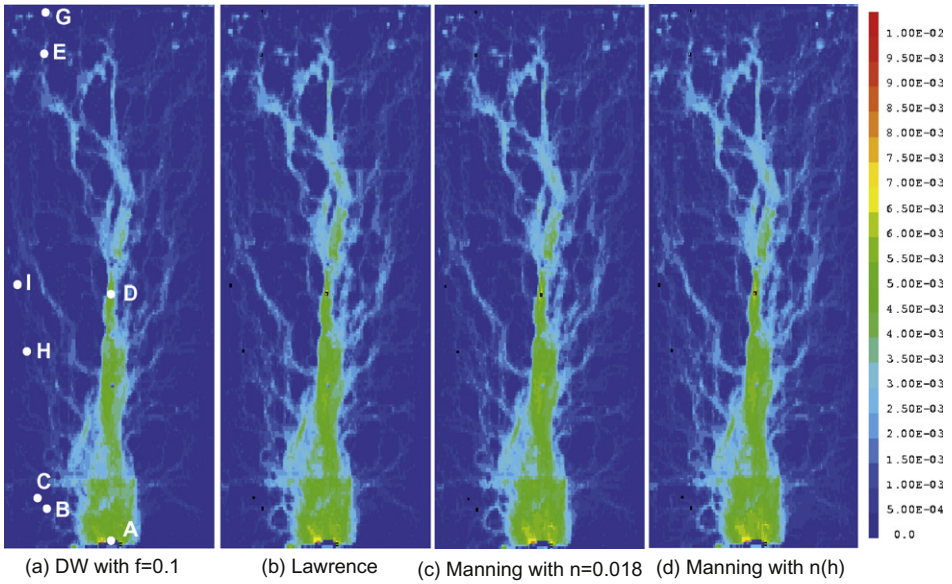

Fig. 6. Water depth (m) calculated with (a) Darcy-Weisbach's model with f constant equal to 0.1; (b) Lawrence's model with $P = 13\%$ and $h_c = 0.5$ mm. (c) Manning's model with n constant equal to 0.018; (d) Manning's model with $n(h)$ given by Eq. (6) with $n_0 = 0.018$, $h_0 = 3$ mm and $\varepsilon = 1/3$.

Calibration of Manning's coefficients gives $n = 0.018$ in the case of a constant n (Fig. 4c) and $n_0 = 0.018$ in the case of the variable $n(h)$ (Fig. 4d). These values are the same because in the main rill where the water depth is high, $n(h)$ reaches the threshold value n_0. Because of the experiment calendar (Table 2), the soil during the tracer experiment may be less compacted than during the velocity experiment. Moreover, successive intensive rainfalls may have crusted the soil surface. Whatever the cause, the hydrograph rise was steeper in the velocity experiment than in the tracer experiment (Weill, 2007). As a consequence, friction factors have likely been higher during the tracer experiment than during the velocity experiment. This conjecture is consistent with Sepaskhah and Bondar (2002) who estimated the Manning roughness coefficient n for bare furrows irrigation. They showed that n was correlated with the number of irrigation and the inflow rates and decreased by about 60–70% after only three irrigations.

3.2.2. Flow characteristics

Fig. 5 gives friction factors as a function of water depth for the four following calculations: DW's model with $f = 0.1$, Lawrence's model with f given by Eqs. (2)–(4) with $P = 13\%$ and $h_c = 0.5$ mm, Manning's model with $n = 0.018$ and f defined as $8gn^2h^{-1/3}$ and Manning's model with $n(h)$ given by Eq. (6) with $n_0 = 0.018$, $h_0 = 3$ mm and $\varepsilon = 1/3$. Figs. 6–9 show the spatial distributions of water depth, friction coefficient, velocity and flux obtained with the four models. Patterns in the water depth maps are quite similar and exhibit a large main channel at the middle of the plot where several lateral smaller rills or furrows converge (see Fig. 6). As the various parameters of the four models were calibrated from the breakthrough curve for injection point D, which was located in the main channel, where the water depth lies between 3 and 7 mm (Fig. 6), the friction factor values are quite similar and approximately equal to 0.1 for this range of h (Figs. 5 and 7). On the contrary, for water depth less than 3 mm, friction coefficient values are much more variable. As quantitatively shown in Fig. 5 and illustrated in Fig. 7, the friction map obtained with Manning's model with $n(h)$ is very contrasted and exhibits very high values outside the rills. According to Figs. 7 and 8, the greater roughness, the smaller velocity.

These steady-state flows have been used to calculate the transport of tracer injected at various points noted D, E, G, H and I in Fig. 6.

3.2.3. Breakthrough curves

Figs. 10–13 give the tracer breakthrough curves. For each model, except for the Manning's model with $n(h)$, we did not succeed to simulate the five tracer experiments with the same set of parameters. Fig. 10 gives the results obtained with Darcy-Weisbach's model with four friction factor f values: $f = 0.1$, 0.2, 0.4 and 0.6. Tracer simulated with DW's model with $f = 0.1$ always travels faster than the tracer simulated with $f = 0.2$, 0.4 or 0.6. This result reflects the simple fact that the greater the roughness, the slower the velocity, and consequently, the slower the tracer. Table 6 gives the tracer arrival time at the plot outlet for the injection points D, E, G, I and H. The three values correspond to the time at which the arrived mass reached 1%, the mass flux was maximum, and the arrived mass reached 99%, respectively. Table 6 shows how strong is the impact of roughness on the arrival time of the tracer at the bottom of the plot. As already presented in Fig. 4, the tracer injected in the main channel at point D was correctly simulated with $f = 0.1$ (red curves[4] in Fig. 10). A value $f = 0.2$ allowed to simulate the breakthrough curve for injection point E (green curves in Fig. 10). As points D and E are located in the main rill, the tracer injected at D or at E mainly travels within areas of high velocity and large water depth. Consequently, the transport of the tracer injected at D and E is better modelled with models having a low friction factor. Oppositely, low value of the friction factor is inappropriate for injections made outside the main rill. Since points G and I are located at source points of runoff, the tracer injected there was firstly transported by very slow flow, then gradually swept along into deeper runoff pathways. Fig. 10 shows that constant friction factor $f = 0.1$ led the tracer injected outside the main rill to travel too fast. Correct values of f for injection points G, I and H (i.e. the upper points) ranged between 0.4 and 0.6.

Similar results were obtained with Manning's model with a constant n. As shown in Fig. 11, the lowest value $n = 0.018$ correctly

[4] For interpretation of colour in Figs. 5, 10–13, the reader is referred to the web version of this article.

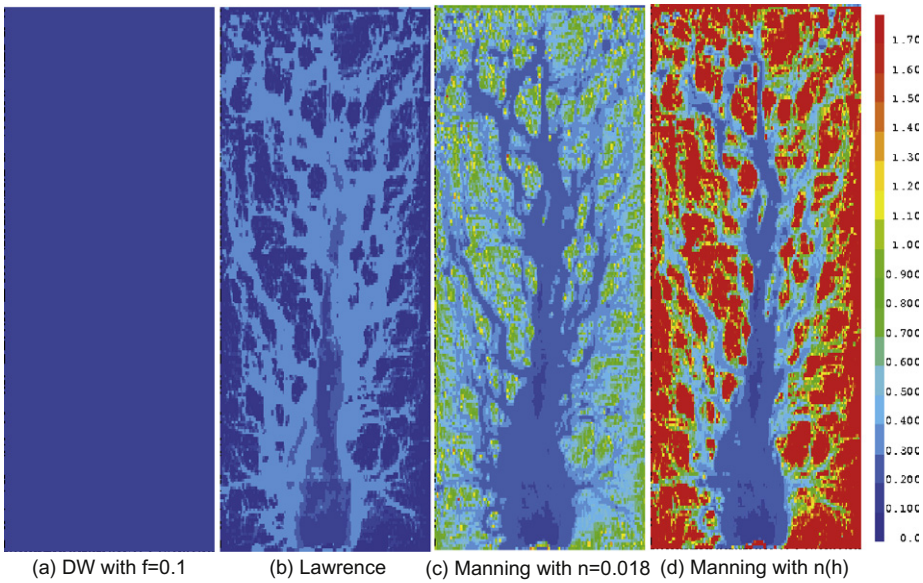

Fig. 7. Friction coefficient calculated with (a) Darcy-Weisbach's model with f constant equal to 0.1; (b) Lawrence's model with $P = 13\%$ and $h_c = 0.5$ mm. (c) Manning's model with n constant equal to 0.018; (d) Manning's model with $n(h)$ given by Eq. (6) with $n_0 = 0.018$, $h_0 = 3$ mm and $\varepsilon = 1/3$.

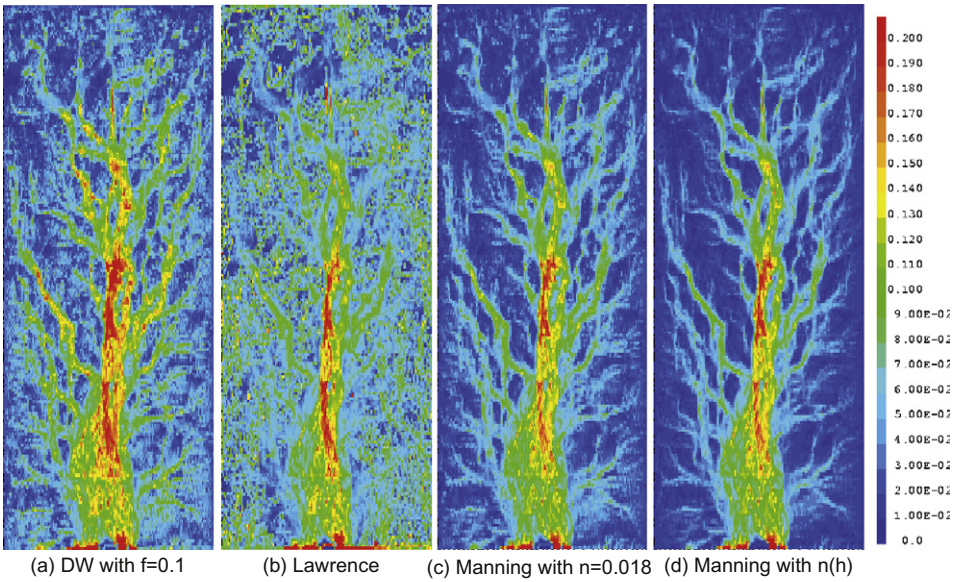

Fig. 8. Velocity (m s^{-1}) calculated with (a) Darcy-Weisbach's model with f constant equal to 0.1; (b) Lawrence's model with $P = 13\%$ and $h_c = 0.5$ mm. (c) Manning's model with n constant equal to 0.018; (d) Manning's model with $n(h)$ given by Eq. (6) with $n_0 = 0.018$, $h_0 = 3$ mm and $\varepsilon = 1/3$.

simulated tracer experiments when the tracer was injected at D or at E (i.e. in the channel) but higher values of n were necessary when the tracer was injected at G and I ($n = 0.025$) or at H ($n = 0.03$). According to Katul et al. (2002) and as done for example in (Thompson et al., 2010), if we assume that the resistance to the flow can be parametrized by relating the microtopography to the momentum roughness height (z_0), the Manning's friction factor n is estimated according to Eq. (5). For 0.5 mm < z_0 < 2.5 mm, we obtain $0.02 < n < 0.025$. This range of values for n is consistent with values obtained from calibration.

Fig. 12 gives breakthrough curves obtained with Lawrence's model. With a characteristic roughness scale h_c fixed to the value of 0.5 mm deduced from calibration at point D (Fig. 4), fractional cover P value had to be taken equal to 13%, 30%, 30% and 100% to correctly simulate the tracer behaviour when injected at E, G, I and H, respectively.

Fig. 13 gives breakthrough curves obtained with Manning's model with a variable $n(h)$. Numerical simulations were performed with h_c and ε values calibrated from surface runoff experiment ($h_c = 3$ mm and $\varepsilon = 1/3$ in Fig. 2d) and the n_0 value calibrated from the breakthrough curve for injection point D ($n_0 = 0.018$ in Fig. 4d). Let us notice here that as good results were qualitatively obtained with $h_0 = 2$ mm, $n_0 = 0.018$ and $\varepsilon = 0.66$. We did not try to solve this problem of equifinality and selected the more coherent values.

3.2.4. Mass recovery

Table 7 gives the mass-recovery percentage of tracer measured at the plot outlet for tracers injected at points D, E, G, I and H. Bold underlined values correspond to sets of model parameters which gave the best fits of tracer breakthrough curves. Whatever the model used, calibrated results are consistent with experimental data: the relative error is about 10% for tracer injected in the main

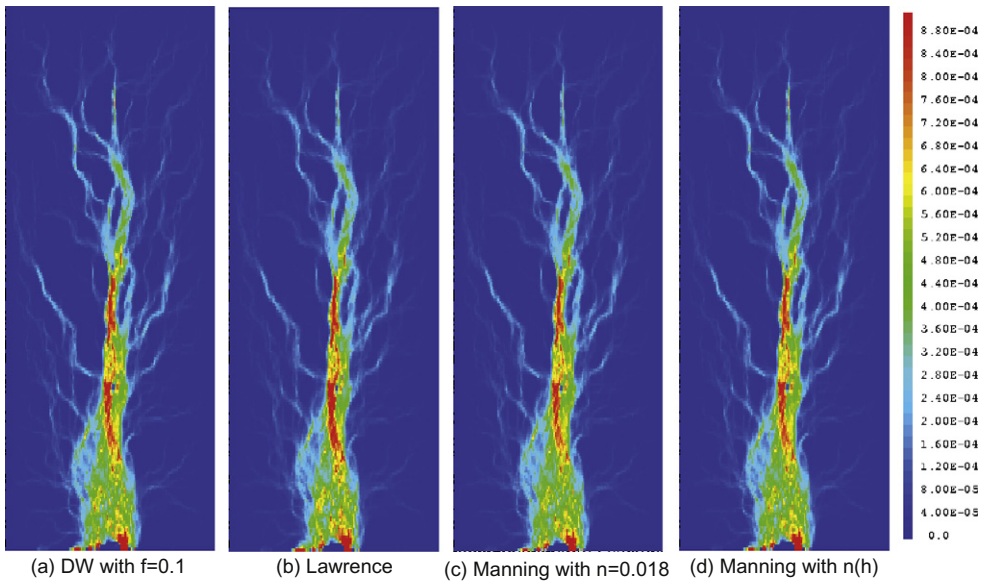

Fig. 9. Flux hu ($m^2\ s^{-1}$) calculated with (a) Darcy-Weisbach's model with f constant equal to 0.1; (b) Lawrence's model with $P = 13\%$ and $h_c = 0.5$ mm. (c) Manning's model with n constant equal to 0.018; (d) Manning's model with $n(h)$ given by Eq. (6) with $n_0 = 0.018$, $h_0 = 3$ mm and $\varepsilon = 1/3$.

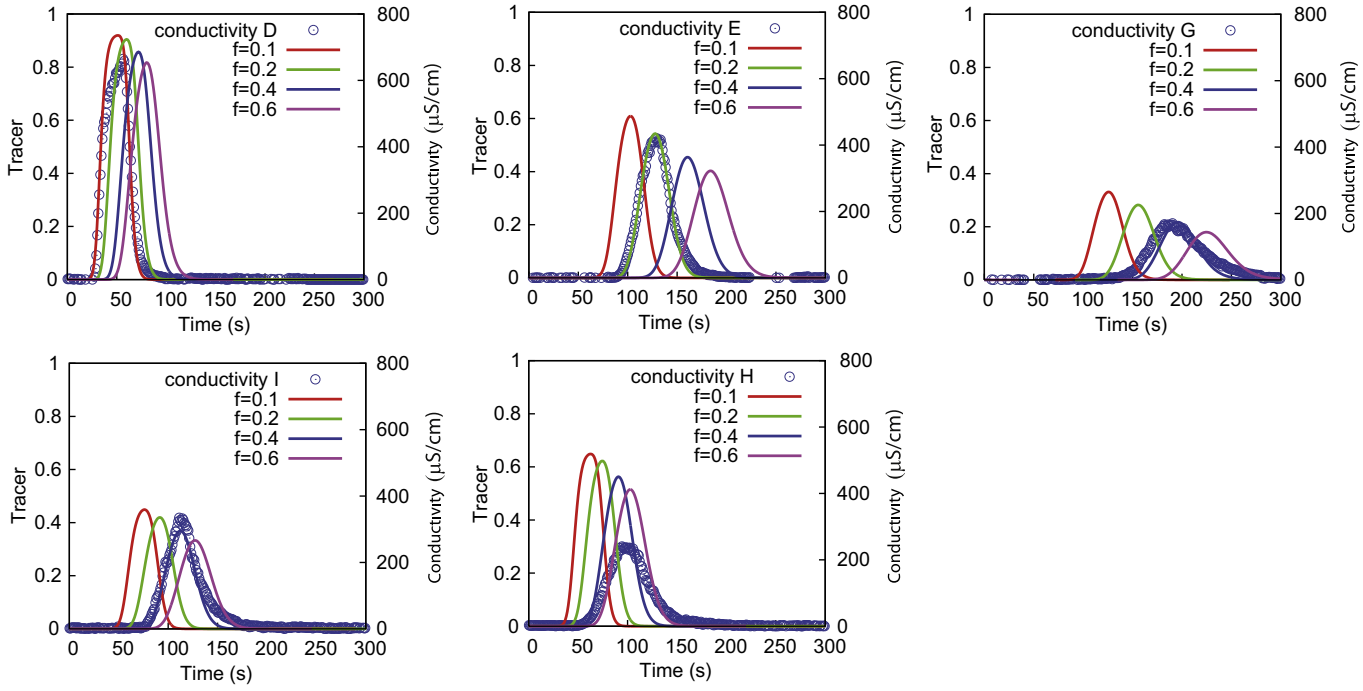

Fig. 10. Breakthrough curves of tracer injected at points D, E, G, I, H. Conductivity data (blue dots) and calibration with Darcy-Weisbach's model with four various constant f values: $f = 0.1$ (red curves), $f = 0.2$ (green curves), $f = 0.4$ (blue curves)and $f = 0.6$ (pink curves).

channel (points D and E) and 20% for the other cases (points G and I). Numerical simulations performed with a coarse DEM ($10 \times 10\ cm^2$ instead of $2.5 \times 5\ cm^2$) demonstrated the sensibility of breakthrough curve to the grid cell size. This dependency is even stronger when the tracer is injected outside the main channel (i.e. at points G, H and I).

4. Discussion

As already mentioned and discussed in (Tatard et al., 2008), the classical DW and Manning-type equations with constant friction slope parameters better model low velocities than higher ones and Tatard et al. (2008) used spatially variable values of the DW friction factor f to enhance the high flow velocities (Fig. 3). This new f field was empirically calibrated against measurements. In our work, we use the heuristic physical model of Lawrence (1997) and the Manning's model with $n(h)$ which both give a spatially variable friction factor (see Eqs. (2)–(4) and Eq. (6)). Fig. 2 shows that the discrepancy between models and measurements at high velocities is globally reduced when the friction slope is modelled according to Lawrence's model or Manning's model with $n(h)$. Furthermore, numerical results are better than those obtained with a heuristic friction coefficient (see Table 4). These results

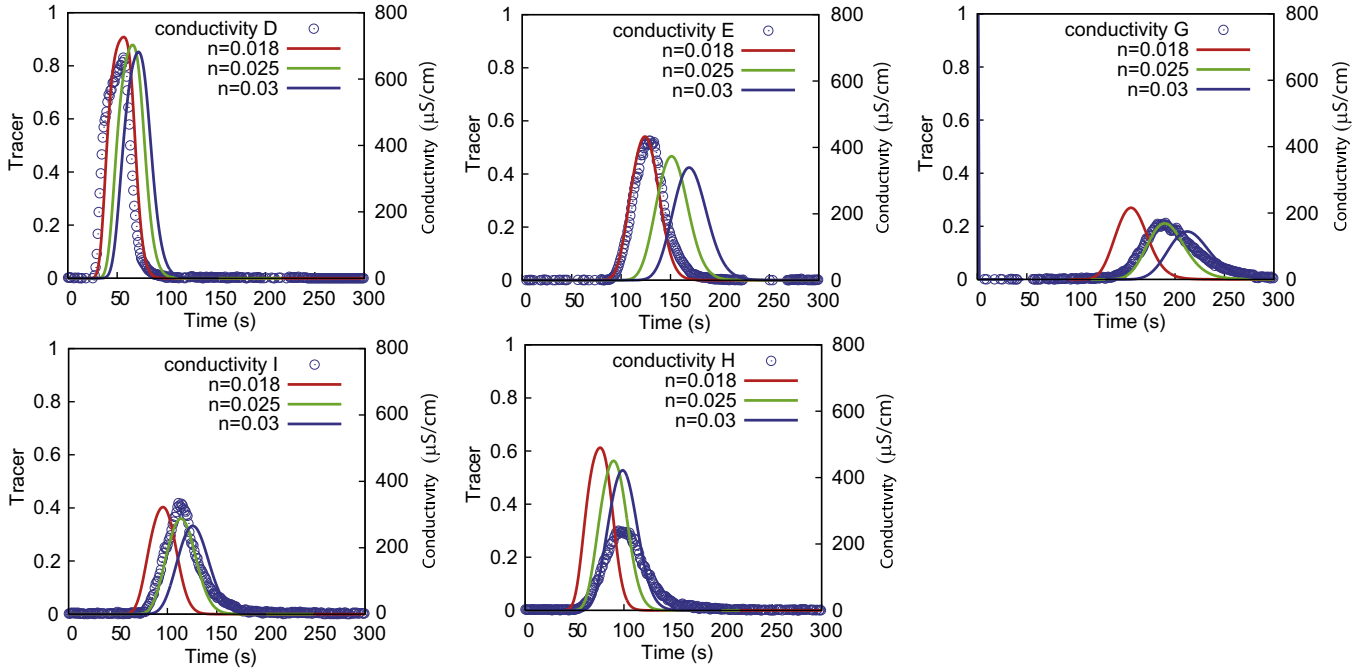

Fig. 11. Breakthrough curves of tracer injected at points D, E, G, I, H. Conductivity data (blue dots) and calibration with Manning's model with three various constant n values: $n = 0.018$ (red curves), $n = 0.025$ (green curves) and $n = 0.03$ (blue curves).

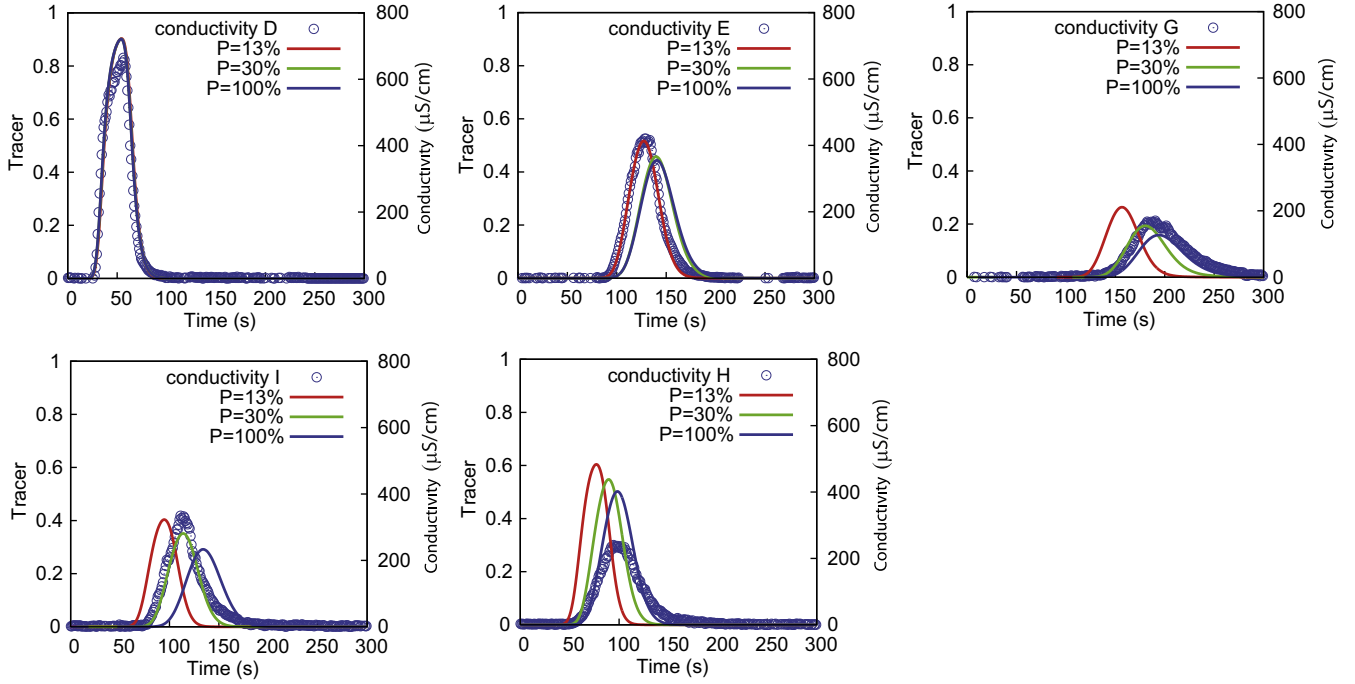

Fig. 12. Breakthrough curves of tracer injected at points D, E, G, I, H. Conductivity data (blue dots) and calibration with Lawrence's model with three various P values: $P = 13\%$ (red curves), $P = 30\%$ (green curves) and $P = 100\%$ (blue curves).

confirm the importance of considering a water-depth dependent friction factor or Manning coefficient in order to correctly simulate local flow velocities. In particular, it enhances the good behaviour of Manning's model with a roughness coefficient decreasing as a power law of the runoff water depth.

Modelling of transport experiment shows that the behaviour of DW's and Manning's models with constant parameters is consistent with results obtained from high-resolution velocity measurements. These have shown that these models are not adequate to model both low and high velocities. The higher the roughness coefficients (f or n), the higher the arrival time of the tracer at the bottom of the plot (see Table 6). It is however interesting to calibrate each transport experiment independently to each other, and to analyze the expected discrepancy between the calibrated friction factors. The results of this numerical experiment are presented in Figs. 10 and 11, which show that satisfying results (although

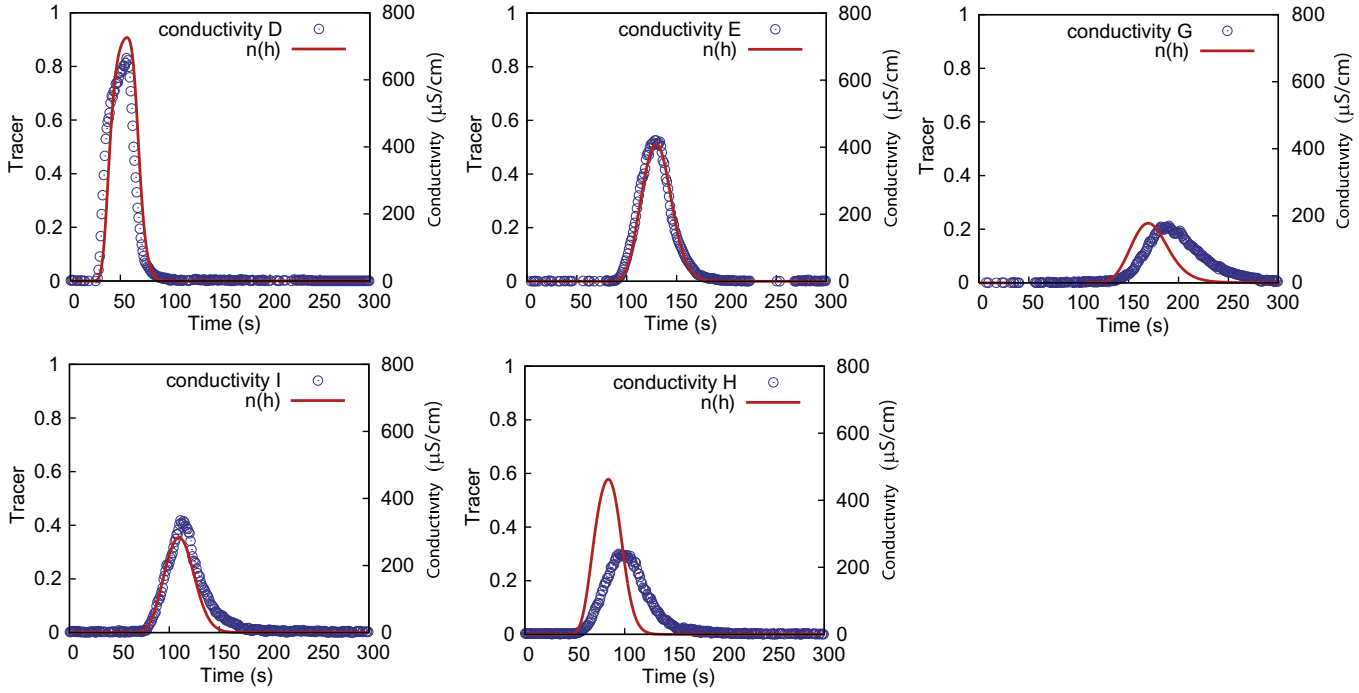

Fig. 13. Breakthrough curves of tracer injected at points D, E, G, I, H. Conductivity data (blue dots) and calibration with Manning's model with $n(h) = 0.018(h/0.003)^{-1/3}$.

Table 6
Tracer arrival time at the plot outlet for the injection points D, E, G, I and H. In each cell of the table the three values correspond to the time at which the arrived mass reached 1%, the mass flux was maximum, and the arrived mass reached 99%, respectively. Bold and underlined values correspond to the best calibrated parameter values.

	Injection at D	Injection at E	Injection at G	Injection at I	Injection at H
Experiment	**27-56-91**	**92-129-180**	**138-182-280**	**78-111-180**	**56-98-180**
Darcy-Weisbach					
$f = 0.1$	**24-51-78**	71-103-137	93-126-165	48-76-105	35-63-90
$f = 0.2$	31-60-91	**93-128-168**	119-156-201	61-92-125	44-74-107
$f = 0.4$	41-72-110	121-161-209	**155-196-250**	**78-112-152**	57-91-130
$f = 0.6$	47-80-123	141-184-238	180-225-286	90-127-172	**66-103-147**
Lawrence					
$h_c = 0.5$ mm, $P = 13\%$	**25-54-86**	**92-127-170**	120-157-204	63-95-129	46-77-111
$h_c = 0.5$ mm, $P = 30\%$	25-54-87	101-140-189	**140-180-239**	**79-114-155**	56-89-130
$h_c = 0.5$ mm, $P = 100\%$	25-54-87	101-141-194	150-194-261	95-134-182	**62-98-126**
Manning					
$n = 0.018$	**28-57-86**	**89-124-165**	119-155-203	64-96-130	46-76-109
$n = 0.025$	35-66-100	112-151-198	**149-190-245**	**79-114-154**	56-90-128
$n = 0.03$	41-72-110	128-169-221	169-212-273	90-126-169	**64-99-141**
Manning with $n(h)$					
$n_0 = 0.018$, $h_0 = 3$ mm, $e = 1/3$	**28-57-87**	**93-129-174**	**130-170-226**	**75-110-151**	**51-84-121**

with parameters not consistent to each other) can be obtained this way. With such parameter values, the average behaviour such as the tracer arrival time and the shape of the breakthrough curve is correct although local characteristics of the flow such as local water depth and local velocity are very likely incorrect. The constant parameter of these models (f for Darcy-Weisbach and n for Manning) allows to model a mean roughness that the tracer encounters along its travel path on the plot surface.

Numerical results obtained with Lawrence's model are more surprising (Fig. 12). On the one hand, calibrated surface-runoff experiment from Lawrence's model are better than those from Darcy-Weisbach's or Manning's models (Fig. 2). On the other hand, here again, a same set of parameters does not allow to simulate the entire set of transport experiments, hence setting the Lawrence model back to the same level as those with constant roughness. Furthermore, DW's and Manning's models have only a single parameter to calibrate while Lawrence's model has two. All of them need a specific set of parameters according to whether tracer is injected in a channel or not. The poor fit of Lawrence's model may be explained by the fact that the tracer travels in zones where, due to the presence of rills of various sizes and depths, roughness varies a lot. The correct simulation of several tracer breakthrough curves with the same flow field implies a good simulation of both velocity and water depth along all the tracer travel path. In Lawrence's heuristic model, soil surface is assumed homogeneous with larger particles periodically distributed. As shown in (Lawrence, 1997), when applied to experimental data, this model exhibits a similar behaviour in average, although with a significant level of scattering. It was also shown that the assumption of individual hemispherical roughness elements relatively uniform in size randomly distributed on a flat surface did not apply to tilled soil surfaces (Takken and Govers, 2000).

Table 7
Mass recovery percentage at the plot outlet for the injection points D, E, G, I and H. Bold and underlined values correspond to best calibrated parameter values.

	Injection at D	Injection at E	Injection at G	Injection at I	Injection at H
Experiment	82	57	44	53	50
Darcy-Weisbach					
$f = 0.1$	**92**	65	39	46	65
$f = 0.2$	92	**63**	37	45	65
$f = 0.4$	91	61	**34**	**44**	64
$f = 0.6$	91	59	32	43	**63**
Lawrence					
$h_c = 0.5$ mm, $P = 13\%$	**92**	**62**	36	44	64
$h_c = 0.5$ mm, $P = 30\%$	93	62	**32**	**43**	63
$h_c = 0.5$ mm, $P = 100\%$	93	63	30	42	**63**
Manning					
$n = 0.018$	**92**	**63**	37	45	64
$n = 0.025$	92	61	**34**	**44**	64
$n = 0.03$	91	60	32	43	**63**
Manning with $n(h)$					
$n_0 = 0.018$, $h_0 = 3$ mm, $\varepsilon = 1/3$	**92**	**63**	**35**	**44**	**64**

Behaviour of Manning's model with a variable $n(h)$ is rather different. Fig. 13 shows that, contrarily to other models, a same set of parameters gives acceptable numerical tracer breakthrough curves whatever the point of injection (except point H). When the tracer is injected in the main channel, it only travels in zones where water depth is higher than h_c: the model behaves like the Manning's model with a constant n equal to 0.018 (see injection at points D and E in Figs. 11 and 13). On the contrary, for injections at G or at I, the tracer encounters various water depths and consequently various soil roughnesses along its travel path.

Whatever the model considered, we did not succeed in simulating the shape of the breakthrough curve for injection point H. We noticed that discrepancy between numerical and experimental results increases with a coarser numerical grid (10×10 cm^2 cells instead of 2.5×2.5 cm^2 cells). So, discrepancy should be attributed to the use of a not enough precise DEM in this zone.

We can notice here that measured breakthrough curves are slightly asymmetric, which was not captured by the models. Asymmetry is mainly due to tracer dispersion. This dispersion can be heterogeneous on the plot. In the transport model, longitudinal and transversal coefficients of dispersion are assumed uniform and constant all over the domain (equal to 0.01 m). Furthermore, infiltration is modelled as a uniform and constant sink term: water which infiltrates is lost for the system.

Tables 6 and 7 show that arrival time of tracer I is shorter than arrival time of tracer E, but its mass recovery is lower. This is due to the fact that tracer injected at I, which is a point located out of main rills, is first transported by dramatically shallow water, and consequently submitted to a great loss of mass by infiltration. Indeed, in a shallow runoff layer the flow velocity is low and the tracer depth-averaged concentration is high, whereas in a thick runoff layer reversed conditions occur. This explains why one can expect higher mass loss in small lateral rills than in the main channel. Table 7 also shows that tracer mass recoveries simulated for a given injection point are very consistent throughout simulations, disregarding the model used and its roughness parameter, with the exception of point G. This observation may be explained by a simple model, given in Appendix A, of a flat plot soil surface with constant slope and steady state runoff. We show there that the tracer mass $M(t)$ is given by:

$$M(t)/M_0 = (X(t,x_0)/x_0)^{-I/(R-I)}, \tag{20}$$

where $X(t,x_0)$ is the position of the tracer injected at time $t = 0$ and point $x = x_0$ (the origin of x is chosen at the top of the plot). This expression shows that in this simplified runoff configuration, the mass of tracer which arrives at a given distance of the injection point is independent of the law which relates runoff velocity to runoff height, while it only depends on the rainfall rate R and the infiltration rate I, equal to 75 mm h^{-1} and 26 mm h^{-1}, respectively. In the case of injection at point D located at 5.31 m from the top of the plot where the runoff has its source, Eq. (20) gives a percentage of tracer arrived at the bottom of the plot ($X = 10$ m) equal to 71%. This value is less than the 81% obtained from measurements because on the real soil surface, all the water which transports the tracer does not flow only in the main channel where the tracer is injected but also arrives from lateral small rills. Tracer is then more diluted in the real 3D experiment than in the academic configuration presented in Appendix A. Consequently, less tracer is lost by infiltration. According to Eq. (A10) in Appendix A, tracer loss can also be written as a function of the flux hu alone. As can be seen in Fig. 9, runoff fluxes hu computed from the four models, each calibrated on breakthrough curve D, are very similar. This explains why mass recovery of each tracer does not depend a lot neither on the model nor on its parameters.

5. Conclusion

This work was based on a series of two rainfall simulation experiments which provided, for the first time at this scale (10-m by 4-m) both high-resolution flow-velocity data (the runoff experiment) and breakthrough curves of tracer injected at several locations (the transport experiment). This dataset has been used to test the four following roughness models:

- Darcy-Weisbach's model characterized by a constant friction factor f.
- Lawrence's model characterized by a characteristic roughness scale h_c and a fractional cover P.
- Manning's model with a constant roughness coefficient characterized by a constant Manning's coefficient n.
- Manning's model with a variable roughness coefficient, characterized by a Manning's water-depth dependent coefficient $n(h)$.

The four models were first tested against local flow-velocity measurements (already simulated by Tatard et al., 2008, with another code). As already mentioned by these authors, models with a constant friction factor largely underestimate high velocities. Oppositely, the heuristic Lawrence's model which intrinsically takes into account the dependence of friction factor with water depth, correctly simulates low and high velocities. Furthermore, the calibration of the Lawrence's model parameters led to values in perfect coherence with measurable characteristics of the soil of the plot: the characteristic roughness scale h_c corresponds to the d_{90} value of the soil granulometry, and the fractional cover P of the model corresponds to the percentage of large grains of sand. Best results, however, were obtained with Manning's model with a water-depth dependent roughness coefficient. With this model, simulation of both low and high velocities was better than from the other tested models, as well as those previously published in Tatard et al. (2008).

Calibration on the transport experiment confirmed the necessity of roughness models with variable parameters: Darcy-Weisbach's model with constant friction factor and Manning's model with constant roughness coefficient required different parametrisation for different injection points, which is not satisfying. Quite surprisingly, Lawrence's model did not succeed better than the constant-roughness models at modelling all tracer experiments

with the same set of parameters. This result shows that even if a model can correctly simulate low and high local velocities, it still can give unsatisfactory results for tracer transport. Manning's model with a roughness coefficient decreasing as a power law of water depth leads to the best calibration. This model allowed to simulate all breakthrough curves with the same set of parameters and results are almost as good as those obtained with the three other models calibrated for each injection point. Furthermore, the set of parameters used to model transport experiments is the same as the set used to model runoff experiments, except the minimum roughness coefficient which is less in the surface runoff experiments. This calibration result is consistent with field evidence of plot surface smoothing between the two experiments.

When tracer is injected in the main rills of the flow pattern, tracer mass recoveries are in good agreement with measurements and seem to be independent of friction laws. This result is confirmed by a simple model showing that the mass decrease of a non reactive tracer transported in the runoff water depth does not depend on the law which relates runoff velocity to runoff water depth.

All these conclusions are drawn for a steady flow. In the case of unsteady rainfall and/or infiltration, the entire wetted surface area can vary with time. As a consequence, flow resistance will vary both with space and time.

Velocity measurements and tracer breakthrough curves performed at the plot scale and presented in (Tatard et al., 2008) and in this paper can be used as benchmarks for overland flow and transport models.

Acknowledgments

The modelling part of the research was conducted at the Commissariat à l'Energie Atomique (CEA, Gif-sur-Yvette). Authors acknowledge Guillaume Nord, from the Laboratoire d'étude des Transferts en Hydrologie et Environnement (LTHE, Grenoble) for fruitful discussions about friction laws. The experimental part was granted by the RIDES project, an ECCO research program, and was hosted by the Ecole Nationale Supérieure d'Agriculture (ENSA) of Thies, Senegal. Authors acknowledge Thierry Bariac, from the laboratory Biogeochimie et Ecologie des Milieux Continentaux (BIOEMCO, Paris), for decisive advices and for putting his isotopic laboratory at our disposal for ^{18}O and ^{2}H analysis. Authors also acknowledge Kokou Abotsi Mensah, from the Institut de Recherche pour le Développement (IRD, Senegal), who built the rainfall simulator. Mbolanoro Rajoelisoa and Lucille Tatard, as Master trainees, did the preliminary data processing of the tracer experiment and preliminary modelling of the runoff experiment, respectively.

Appendix A. Non reactive tracer transport in runoff water depth

Let us study the transport of a non reactive tracer in runoff water produced by a constant rainfall on a 2D soil vertical cut with a constant slope (see Fig. A1).

The runoff water depth $h(x,t)$ is governed by the following water mass balance equation

$$\frac{\partial h}{\partial t}+\frac{\partial}{\partial x}(hu)=R-I, \tag{A1}$$

where $u(x,t)$ is the runoff velocity, R, the recharge and $I(t)$, the infiltration rate. The axis x is aligned with the soil surface.

After integration along the z-axis, the transport equation governing tracer concentration $c(x,t)$ is given by the following depth-averaged equation:

$$\frac{\partial(hc)}{\partial t}+\frac{\partial}{\partial x}(huc)=-Ic, \tag{A2}$$

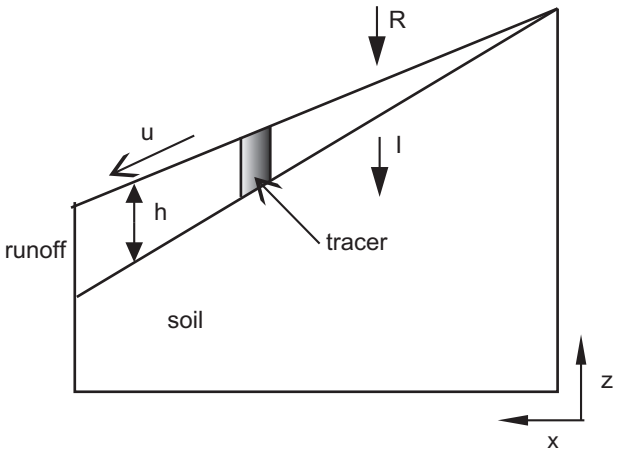

Fig. A1. Sketch of the studied configuration.

where advection is the only transport mechanism taken into account. We assume that vertical mixing of the tracer is instantaneous: concentration is at any time constant along runoff water depth. When runoff steady state is reached, the infiltration rate I becomes constant with time and Eq. (A1) reduces to:

$$hu=(R-I)x. \tag{A3}$$

The transport equation reads:

$$h\frac{\partial c}{\partial t}+hu\frac{\partial c}{\partial x}+Rc=0. \tag{A4}$$

If a mass M_0 of tracer is injected at the initial time $t=t_0$ at the point $x=x_0$, we can write:

$$c(x,t=0)=\frac{M_0}{h_0}\delta(x-x_0), \tag{A5}$$

where $h_0=h(x_0)$. Then the concentration $c(x,t)$ at time t and at the position x is:

$$c(x,t)=\frac{M(t)}{h(X(t,x_0))}\delta(x-X(t,x_0)), \tag{A6}$$

where $X(t,x_0)$ is the tracer position at time t and $M(t)$ is the mass of tracer at that time. As the tracer penetrates into the soil with infiltration water the total mass $M(t)$ decreases with time. This mass is obtained by spatial integration of the transport equation (A1):

$$\int_0^L\frac{\partial(hc)}{\partial t}dx+\int_0^L\frac{\partial}{\partial x}(huc)dx=-I\int_0^L cdx, \tag{A7}$$

where L is the length of the soil surface. Eqs. (A6) and (A7) give:

$$\frac{dM(t)}{dt}=-I\frac{M(t)}{h(X(t,x_0))}, \tag{A8}$$

which can be written as:

$$\frac{dM}{M}=-\frac{I}{h(X)}dt=-\frac{I}{h(X)}\frac{dt}{dX}dX=-\frac{I}{h(X)u(X)}dX. \tag{A9}$$

As a consequence, we have:

$$\frac{M(t)}{M_0}=\exp\left(-\int_{x_0}^{X}\frac{I}{h(x)u(x)}dx\right). \tag{A10}$$

According to Eq. (A3) which gives the velocity u, we may rewrite Eq. (A9) as follows:

$$\frac{dM}{M}=-\frac{I}{(R-I)X}dX. \tag{A11}$$

After integration, we obtain the final result:

$$M(t)/M_0 = (X(t,x_0)/x_0)^{-I/(R-I)}, \quad \text{(A12)}$$

which is independent of the law relating the runoff velocity u to the runoff water depth h.

References

Abrahams, A.D., Parsons, A.J., Luk, S.-H., 1986. Resistance to overland flow on desert hillslopes. J. Hydrol. 88, 343–363.

Andersson, P., Byegard, J., Tullborg, E.-L., Doe, T., Hermanson, J., Winberg, A., 2004. In situ tracer tests to determine retention properties of a block scale fracture network in granitic rock at the Äspö Hard Rock Laboratory, Sweden. J. Contam. Hydrol. 70, 271–297.

Bear, J., Tsang, C.F., de Marsily, G., 1993. Flow and Contaminant Transport in Fractured Rock. Academic Press, San Diego, CA (United States).

Bernard-Michel, G., Le Potier, C., Beccantini, A., Gounand, S., Chraibi, M., 2004. The Andra Couplex 1 test case: comparisons between finite-element, mixed hybrid finite element and finite volume element discretizations. Comput. Geosci. 8, 187–201.

Chow, V.T., Maidment, D.R., Mays, L.W., 1988. Applied Hydrology. McGraw-Hill, New-York (NY, USA). 572p.

Dabbene, F., 1998. Mixed hybrid finite elements for transport of pollutants by underground water. In: Proceedings of the 10th Int. Conf. on Finite Elements in Fluids, Tucson, USA.

Darboux F., 2011. Personal communication.

De Roo, A.P.J., Hazelhoff, L., Burrough, P.A., 1989. Soil erosion modelling using «ANSWERS» and geographical information systems. Earth Surf. Process. Land. 14, 517–532.

Esteves, M., Planchon, O., Lapetite, J.M., Silvera, N., Cadet, P., 2000a. The 'EMIRE' large rainfall simulator: design and field testing. Earth Surf. Process. Land. 25, 681–690.

Esteves, M., Faucher, X., Galle, S., Vauclin, M., 2000b. Overland flow and infiltration modelling for small plots during unsteady rain: numerical results versus observed values. J. Hydrol. 228, 265–282.

Grisak, G.E., Pickens, J.F., 1981. An analytical solution for solute transport through fractured media with matrix diffusion. J. Hydrol. 52, 47–57.

Jain, M.K., Kothyari, U.C., Ranga Raju, K.G., 2004. A GIS distributed rainfall–runoff model. J. Hydrol. 299, 107–135.

Jain, M.K., Singh, V.P., 2005. DEM-based modelling of surface runoff using diffusion wave equation. J. Hydrol. 302, 107–126.

Kadlec, R.H., 1990. Overland flows in wetlands: vegetation resistance. J. Hydraul. Eng. 116 (5), 691–706.

Katul, G., Wiberg, P., Albertson, J., Hornberger, G., 2002. A mixing layer theory for flow resistance in shallow streams. Water Resour. Res. 38 (11), 1250. doi:10.1029/2001WR000817.

Kirby, M.J., 1978. Hillslope Hydrology. Wiley, New York.

Lawrence, D.S.L., 1997. Macroscale surface roughness and frictional resistance in overland flow. Earth Surf. Process. Land. 22, 365–382.

Lawrence, D.S.L., 2000. Hydraulic resistance in overland flow during partial and marginal surface inundation: experimental observations and modeling. Water Resour. Res. 36 (8), 2381–2393.

McGuire, K.J., Weiler, M., McDonnell, J.J., 2007. Integrating tracer experiments with modeling to assess runoff processes and water transit times. Adv. Water Resour. 30, 824–837.

Morris, E.M., Woolhiser, D.A., 1980. Unsteady one-dimensional flow over a plane: partial equilibrium and recession hydrographs. Water Resour. Res. 16 (2), 355–360.

Mouret, G., 1921. Antoine chézy: history of a hydraulic formula (in French). Ann. Ponts Chaussées 61, 165–269.

Moussa, R., Bocquillon, C., 1996. Criteria for the choice of flood-routing methods in natural channels. J. Hydrol. 186, 1–30.

Moussa, R., Bocquillon, C., 2000. Approximation zones of the Saint-Venant equations for flood routing with overbank flow. Hydrol. Earth Syst. Sci. 4, 251–261.

Pearson, C.P., 1989. One-dimensional flow over a plane: criteria for kinematic wave modelling. J. Hydrol. 111, 39–48.

Planchon, O., Esteves, M., Silvera, N., Lapetite, J.-M., 2000. Raindrop erosion of tillage induced microrelief: possible use of the diffusion equation. Soil Tillage Res. 56, 131–144.

Planchon, O., Esteves, M., Silvera, N., Lapetite, J.-M., 2001. Microrelief induced by tillage: measurement and modelling of surface storage capacity. Catena 46, 141–157.

Planchon, O., Silvera, N., Gimenez, R., Favis-Mortlock, D., Wainwright, J., Le Bissonnais, Y., Govers, G., 2005. An automated salt-tracing gauge for flow-velocity measurement. Earth Surf. Process. Land. 30, 833–844.

Rai, R.K., Upadhyay, Alka., Singh, V.P., 2010. Effect of variable roughness on runoff. J. Hydrol. 382, 115–127.

Sepaskhah, A.R., Bondar, H., 2002. Estimation of Manning roughness coefficient for bare and vegetated furrow irrigation. Biosyst. Eng. 82 (3), 351–357.

Singh, V.P., Aravamuthan, V., 1996. Errors of kinematic-wave and diffusion-wave approximations for steady-state overland flows. Catena 27, 209–227.

Smith, M.W., Cox, N.J., Bracken, L.J., 2007. Applying flow resistance equations to overland flows. Prog. Phys. Geogr. 31, 363–387.

Tatard, L., Planchon, O., Wainwright, J., Nord, G., Favis-Mortlock, D., Silvera, N., Ribolzi, O., Esteves, M., Huang, Chi.Hua., 2008. Measurement and modelling of high-resolution flow-velocity data under simulated rainfall on a low-slope sandy soil. J. Hydrol. 348, 1–12.

Takken, I., Govers, G., 2000. Hydraulics of interrill overland flow on rough, bare soil surfaces. Earth Surf. Process. Land. 25, 1387–1402.

Thompson, S.E., Katul, G.G., Porporato, A., 2010. Role of microtopography in rainfall–runoff partitioning: an analysis using idealized geometry. Water Resour. Res. 46, W07520. doi:10.1029/2009WR008835.

Tsihrintzis, V.A., 2001. Discussion on Variation of roughness coefficients for unsubmerged and submerged vegetation. Hydraul. Eng. 2001, 241–245.

Wasantha Lal, A.M., 1998. Weighted implicit finite-volume model for overland flow. ASCE J. Hydraul. Eng. 124, 941–950.

Weill, S., 2007. Modélisation des échanges surface/subsurface à l'échelle de la parcelle par une approche darcéenne multidomaine. PhD thesis of École des Mines de Paris (France).

Weill, S., Mouche, E., Patin, J., 2009. A generalized Richards equation for surface/subsurface flow modelling. J. Hydrol. 366, 9–20.

Woolhiser, D.A., Liggett, J.A., 1967. Unsteady, one-dimensional flow over a plane – the rising hydrograph. Water Resour. Res. 3 (3), 753–771.

Zhang, W., Cundy, T.W., 1989. Modeling of two-dimensional overland flow. Water Resour. Res. 25 (9), 2019–2035.

Wu, F.-C., Shen, H.W., Chou, Y.-J., 1999. Variation of roughness coefficients for unsubmerged and submerged vegetation. J. Hydraul. Eng. 125 (9), 934–942.